PHYSICAL SCIENCES

A photon-recycling incandescent lighting device

Heng Zhang[1], Zhequn Huang[2], Min Ding[3], Qixiang Wang[1], Yilin Feng[1], Zhenghong Li[4], Shan Wang[4], Lei Yang[5], Shuai Chen[5], Wen Shang[1], Jian Zhang[6], Tao Deng[1], Hongxing Xu[7], Kehang Cui[1]*

Energy-efficient, healthy lighting is vital for human beings. Incandescent lighting provides high-fidelity color rendering and ergonomic visual comfort yet is phased out owing to low luminous efficacy (15 lumens per watt) and poor lifetime (2000 hours). Here, we propose and experimentally realize a photon-recycling incandescent lighting device (PRILD) with a luminous efficacy of 173.6 lumens per watt (efficiency of 25.4%) at a power density of 277 watts per square centimeter, a color rendering index (CRI) of 96, and a LT70-rated lifetime of >60,000 hours. The PRILD uses a machine learning–designed 637-nm-thick visible-transparent infrared-reflective filter and a Janus carbon nanotube/hexagonal boron nitride filament to recycle 92% of the infrared radiation. The PRILD has higher luminous efficacy, CRI, and lifetime compared with solid-state lighting and thus is promising for high–power density lighting.

INTRODUCTION

Lighting takes approximately 20% of global electricity consumption and more than 10% of carbon emission (*1*, *2*). Increasing the lighting efficiency plays a major role in achieving future carbon neutrality. Solid-state lighting (SSL), such as light-emitting diode (LED)–based lighting and laser diode (LD)–based lighting, converts electricity to luminous flux with high efficiency by electroluminescence. SSL is the prevailing lighting technology at two ends of the power density spectrum: LED-based lighting works efficiently at low–input power density below 5 W/cm^2, while LD-based lighting operates efficiently at high–input power density above a threshold of 4 kW/cm^2. In between is "the valley of efficiency droop" (*3*), where the severe thermal (dissipation) (*4*, *5*) and nonthermal (Auger) (*3*) efficiency degradation limits the capability to produce photons per unit area of a semiconductor chip. Moreover, SSL relies on phosphorescent down-converters to broaden its emission band in the visible range, which generates heat and introduces a trade-off between efficacy and color fidelity. Retaining a high luminous efficacy would result in color distortion [low color rendering index (CRI) below 80] and strong blue light emission, causing potential damage to the human health (*6*–*8*) and the ecosystem (*9*–*11*).

Compared with SSL, the natural lighting from incandescence has continuous, full spectrum in the visible range, providing high color fidelity and ergonomic comfort for human beings. Through generations of engineering optimization, tungsten wire stands out as the choice of filament material for incandescent lighting because of its high melting temperature, low vapor pressure, and selectivity in thermal emission. However, even with techniques such as alloying, ceramic protection, and halogen regeneration, the lifetime of the tungsten filament is still limited to 2000 hours (*12*), which is approximately an order of magnitude lower than that of SSL (~20,000 hours) (*13*). As the electrical resistance of the tungsten filament varies notably (~20 times) between the cold (off) state and the hot (on) state, the current overload at the cold state often leads to its premature failure. Furthermore, as the majority of the emitted power from the tungsten filament is in the infrared range, the luminous efficacy of the incandescent lighting remains below 15 lumens (lm)/W (luminous efficiency <2%), which is much lower than that of the SSL (luminous efficacy > 100 lm/W). Previous conceptual demonstration of tailoring thermal radiation using photonic crystal or interference filter (*14*–*17*) increases the luminous efficacy of the incandescent lighting to 45 lm/W (efficiency of 6.6%), which is still far inferior to those of the state-of-the-art SSL (140 to 160 lm/W) (*13*). Besides, the lifetime issue of the tungsten filament remains unsolved. Incandescent lamps are thus phased out because of the short lifetime and the low luminous efficacy.

Here, we propose and experimentally realize a photon-recycling incandescent lighting device (PRILD) that has high luminous efficacy, high luminance, high color fidelity, ergonomically comfortable color temperature, long lifetime, excellent reliability, low environmental impact, low carbon footprint, and low cost. We also aim to fundamentally overcome the long-standing inherent bottlenecks of SSLs, including the efficiency droop (trade-off between luminous efficacy and luminance), the trade-off between luminous efficacy and color fidelity, the blue light pollution, as well as thermal management and operation reliability.

RESULTS

Photon-recycling incandescent lighting device

The schematic of the PRILD is shown in Fig. 1A. The filament of the PRILD is an all-ceramic Janus thermal emitter (JTE) strip (Fig. 1B), which consists of a hexagonal boron nitride (hBN) white emitter and a carbon nanotube (CNT) black emitter (see Materials and Methods and fig. S1). The JTE is suspended inside of a ceramic corundum cavity (CCC). A quartz window with an omnidirectional visible-transparent infrared-reflective filter (VTIRF), named as VTIRF window, is placed below the CNT black emitter. The photon-recycling scheme of the PRILD works as follows. The

[1]School of Materials Science and Engineering, State Key Laboratory of Metal Matrix Composites, Center for Hydrogen Science, Shanghai Jiao Tong University, Shanghai 200240, China. [2]Zhiyuan Innovative Research Center, Shanghai Jiao Tong University, Shanghai 200240, China. [3]Shanghai HeiYi Materials Technology Co. Ltd., Shanghai 200240, China. [4]Shanghai IdeaOptics Co. Ltd., Shanghai 200433, China. [5]Tianjin H-Chip Technology Group Corporation, Tianjin 300467, China. [6]Research Center for Transparent Ceramics, Shanghai Institute of Ceramics, Chinese Academy of Sciences, Shanghai 200050, China. [7]Institute of Advanced Studies, School of Physics and Technology, Wuhan University, Hubei 430072, China.
*Corresponding author. Email: cuikehang@sjtu.edu.cn

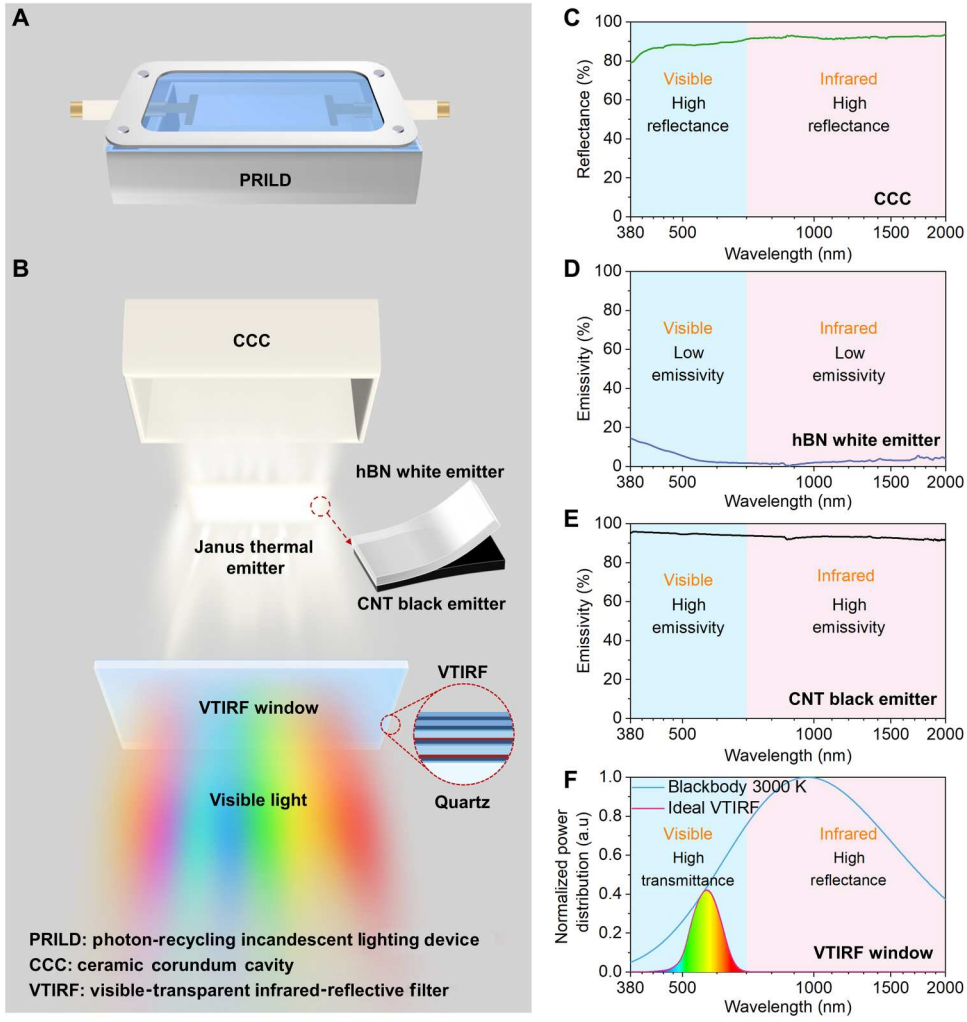

Fig. 1. PRILD system design. (**A**) Device assembly of the PRILD. (**B**) Schematic of key components of the PRILD, including an omnidirectional reflective ceramic corundum cavity (CCC), a Janus thermal emitter (JTE) consisting a hBN white emitter and a CNT black emitter, and a visible-transparent infrared-reflective filter (VTIRF) window. (**C**) Experimentally measured reflectance of the CCC. (**D**) Experimentally measured emissivity of the hBN white emitter. (**E**) Experimentally measured emissivity of the CNT black emitter. (**F**) Desired optical properties of the ideal VTIRF window: high transmittance in the visible range and high reflectance in the infrared range. The spectra of photopic luminosity function (human eye sensitivity curve) and blackbody radiation intensity at 3000 K are also shown.

fabricated hBN white emitter has low emissivity in the visible and near-infrared (NIR) ranges (measured spectrum shown in Fig. 1D), which cuts the energy flow toward the device cavity. The parasitic radiation from the hBN white emitter is further compensated by the full-spectrum high reflectivity of the fabricated CCC (measured spectrum shown in Fig. 1C). The hBN white emitter and the CCC form the inner circle of photon recycling, resulting in unidirectional transmission of energy and suppression of energy dissipation loss in the device cavity. The fabricated CNT black emitter has near-unity emissivity in the visible and infrared ranges (measured spectrum shown in Fig. 1E), which enables high luminous intensity and CRI (*18*). The refractory ceramic nature (*19*, *20*) of the JTE and the CCC intrinsically elongates the lifetime of the PRILD. The VTIRF faces toward the CNT side of the JTE, serving as the gate of photon flow management, which transmits radiation in the visible range and reflects radiation in the ultraviolet (UV) and NIR ranges (ideal spectrum shown in Fig. 1F). The reflected UV and NIR radiation would be reabsorbed by the CNT black emitter, accomplishing the device-level photon recycling.

Design and fabrication of the VTIRF

The VTIRF needs to fulfill the following requirements: (i) omnidirectional transmittance in the visible wavelength range for high luminous intensity and CRI, (ii) omnidirectional reflectance in the UV wavelength range and the infrared wavelength range for high luminous efficacy and effective photon recycling, (iii) minimal optical absorption in the whole spectrum to avoid absorption-induced heat dissipation loss, and (iv) fabrication scalability and cost-effectiveness. The remarkable contrast in optical properties between the adjacent wavelength ranges and the broadband reflection pose unprecedent challenges for the computational design of the VTIRF.

Conventional optical filters based on lossless dielectric stacks, such as photonic crystals, chirped mirrors, and distributed Bragg

reflectors, have narrow reflection bandwidths and suffer from strong oscillations near the band edges. Superimposing multiple filters (*14*) could broaden the reflection bandwidth. However, this will require hundreds of layers with a millimeter-scale thickness, resulting in accumulation of nonstoichiometry and impurity-mode photothermal losses as well as high manufacturing costs for scale-up lighting applications.

In this work, the optical control scheme of the VTIRF is designed as follows: (i) leveraging the perfect conductor property of Ag-Ge alloy to achieve omnidirectional broadband reflection in the infrared range, (ii) suppressing the localized and propagating surface plasmon resonance to mitigate the optical loss of Ag-Ge alloy, and (iii) matching the impedance of the VTIRF with air to reduce the reflection in the visible range. Considering the fabrication scalability and complexity, we adopt a one-dimensional (1D) multilayer stack that comprises four materials: three dielectric materials—HfO_2, Al_2O_3, and SiO_2 with high, medium, and low dielectric constants, respectively—and a conductor material Ag-Ge alloy. We limit the total filter thickness to less than 800 nm and the layer number to less than 15. The thickness of each layer is restrained in the range of 0 to 200 nm and is designed with the precision of 0.01 nm. The estimated design space consists of 6.2×10^{71} candidates.

We use a machine learning–enabled multiobjective optimization framework to computationally search the desired VTIRF structure. An elitist nondominated sorting genetic algorithm II (NSGA-II) (*21*) combined with the transfer matrix method (TMM) is used for the multiobjective optimization (see Materials and Methods). The elitist principle and nondomination diversity preservation of the NSGA-II algorithm would enable efficient realization of the global optimal solution set with randomly generated initial population. In the framework, the three optimization objectives are set as follows: (i) obj_{eff} to evaluate the average deviation between the transmittance of the designed structure and the perfect transmittance, (ii) obj_{CRI} to evaluate the flatness of the transmittance curve in the visible range, and (iii) obj_{loss} to evaluate the absorption loss in the VTIRF. The optimal VTIRF structure is obtained by analyzing the 3D Pareto optimal front of the evolving generations. For visual clarity, the 3D Pareto front is projected onto three 2D planes, as shown in Fig. 2 (A to C). The computational search takes only 6 hours to evolve 80 generations on a moderate workstation (3.2-GHz CPU, 56 cores, and 128-GB memory). After 80 generations of evolution, the deviation between the ideal and the designed properties is less than 5% for all the three objectives.

We further screen the champion solution set from the 200 Pareto front solution sets by balancing the luminous efficacy, CRI, and fabrication feasibility. The chosen structure (red star marked in Fig. 2, A to C) has 11 layers and a total thickness of 637 nm. The thickness of each layer is 25.71 nm (HfO_2), 11.74 nm (Ag-Ge alloy), 107.10 nm (SiO_2), 14.59 nm (HfO_2), 11.91 nm (Ag-Ge alloy), 130.66 nm (SiO_2), 9.74 nm (Al_2O_3), 78.12 nm (HfO_2), 125.49 nm (Al_2O_3), 58.13 nm (HfO_2), and 64.22 nm (Al_2O_3), as depicted in fig. S2. The designed VTIRF has a photopic weighted transmittance of 75% in the visible range (Fig. 2D) and a broadband averaged reflectance of 93% in the infrared range (Fig. 2E), with a sharp cutoff transition from the high transmittance band to the high reflectance band. By integrating the transmittance spectrum with the photopic function, the designed VTIRF theoretically enables a luminous efficacy of 236 lm/W (luminous efficiency of 34.5%) and a CRI of 96 for an ideal PRILD that operates at 3000 K.

We investigate the underlying mechanism of the optical control in the designed VTIRF. First, the electric field distribution in Fig. 2F shows that the surface plasmon resonance of the Ag-Ge layers is effectively suppressed by the HfO_2 layers with the large dielectric constant, resulting in the quenched nonradiative dissipation loss (left panel of the third column in fig. S4). Second, we calculate the complex admittance diagrams at the wavelengths of 455 nm (fig. S5B), 545 nm (Fig. 2G), and 631 nm (fig. S5H). At the three wavelengths, the end points of the VTIRF structure are close to (1, 0) on the diagrams, demonstrating good impedance matching with air, which substantially reduces the reflectance. Third, the destructive interference (fig. S3) from the five-layer HfO_2/Al_2O_3 dielectric stack on top sharpens the cutoff transition from the high transmittance band to the high reflectance band. Fourth, the broadband infrared reflectance is achieved by the metallic feature of the Ag-Ge alloy. The four mechanisms synergistically contribute to the optical performance of the VTIRF.

We then fabricate the VTIRF on a 3-mm-thick quartz substrate using atomic layer deposition and electron beam evaporation (see Materials and Methods). The fabricated VTIRF window is uniform and highly transparent and appears a light blue color (Fig. 3A). The spectroscopic ellipsometry mapping shows that its thickness is uniform throughout the fabricated VTIRF window (fig. S6). The experimentally measured transmittance of the fabricated VTIRF sample matches well with the design (Fig. 3B), with a transmittance of 78% at the peak photopic sensitive wavelength. As a reference, the transmittance of the quartz substrate is 93%. Moreover, the fabricated VTIRF window shows angle-independent transmittance from 0° to 60° (Fig. 3C). Under the infrared thermal camera (Fig. 3D), the fabricated VTIRF window shows a very low thermal emissivity and blocks almost all the infrared radiation, demonstrating infrared stealth characteristics. The fabricated VTIRF window has a total hemispherical reflectance of 92% in the infrared range (Fig. 3E), and an omnidirectional high reflectance at incident angles from 0° to 60° (Fig. 3F). On the basis of the Kirchhoff law, the averaged absorption loss of the fabricated VTIRF window in the visible and NIR ranges is measured as 6% (fig. S7). Both the measured transmittance and reflectance spectra of the fabricated VTIRF match well with those of the designed VTIRF in the visible and NIR ranges.

We build the PRILD by assembling the fabricated CCC, the fabricated JTE, and the fabricated VTIRF window. The light emission spectra of the operating PRILD are measured using fiber optic spectrometers (see Materials and Methods). The schematic of the measurement setup is shown in fig. S8. The temperature of the JTE is monitored by an infrared pyrometer sensor, and the relationship between the temperature and the electrical resistance is recorded (see Materials and Methods and fig. S9). The operating temperature of the PRILD is 2457 K. The PRILD in operation (photograph in the inset of Fig. 4A) emits warm yellow light in CIE 1931 color space (*22*), with a CRI of 96 and a correlated color temperature (CCT) of 2614 K (see fig. S10 for more details). The CCT is slightly higher than the temperature of the JTE, which is attributed to the higher reflection of the red color by the VTIRF. The power-up delay of the PRILD is only 46 ms (fig. S11A), which is much shorter than that of the conventional incandescent bulbs (ca. 0.15 s) (*23*). The corresponding heating and cooling rates of the JTE are ca. 40,000 and 6500 K/s, respectively (fig. S11B). The fast switch-on and

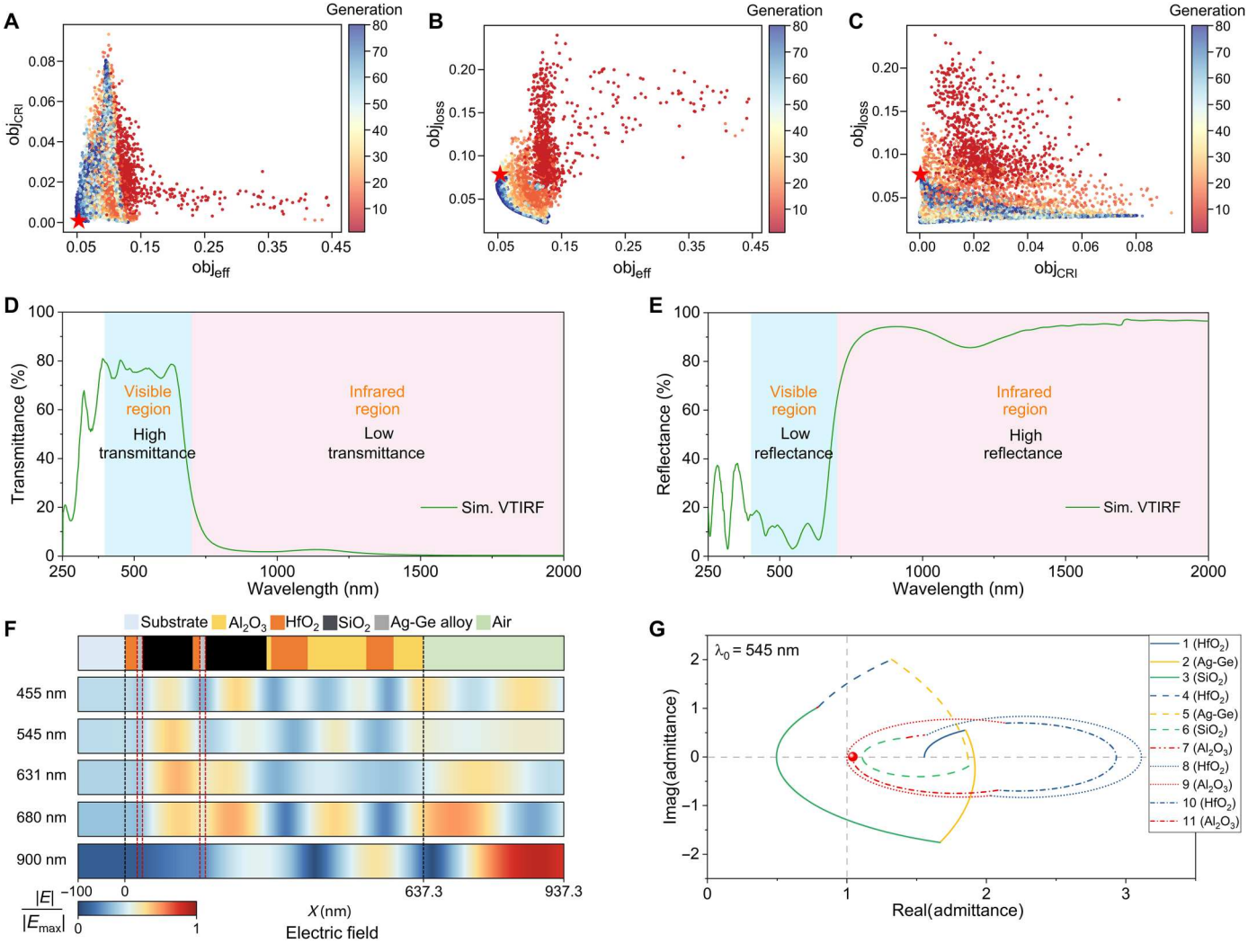

Fig. 2. VTIRF design. (**A** to **C**) Projections of 3D Pareto front onto three 2D planes obtained by the machine learning–enabled multiobjective optimization. Each axis represents one of the three objective functions (obj_{eff}, obj_{CRI}, and obj_{loss}). (**D**) Calculated transmittance spectrum of the designed VTIRF. (**E**) Calculated reflectance spectrum of the designed VTIRF. (**F**) Electric field distribution of the VTIRF at the wavelengths of 455, 545, 631, 680, and 900 nm. The black dashed line marks the location of the VTIRF, while the red dashed line marks the location of the Ag-Ge layer. A more detailed comparison of electric field, magnetic field, and Poynting vector at other wavelengths is provided in fig. S4. (**G**) Optical admittance diagram of the designed VTIRF at the wavelength of 545 nm. Optical admittance diagrams at other wavelengths are provided in fig. S5.

switch-off response of the PRILD is attributed to the low thermal mass of the JTE.

Figure 4A illustrates the normalized light emission spectrum of the PRILD at the operating temperature of 2457 K. The majority of the light emission is in the visible range, and the emission in the infrared range is quenched below 6%. The fabricated VTIRF window reflects 92% of the JTE-emitted infrared photons (shaded in yellow in Fig. 4B), which are scavenged by the CNT side of the JTE to complete the photon recycling. The blockage of the infrared photons notably increases the luminous efficacy. At 2457 K, the experimentally measured luminous efficacy of the PRILD is 173.6 lm/W (Fig. 4C), at an input power density of 277 W/cm^2 (current density of 2.4 kA/cm^2). Owing to the high power density and luminous efficacy, the luminance of the operating PRILD reaches 904,483 cd/m^2, which is much higher than the state-of-the-art LED lighting (table S1). The luminous efficacy of the PRILD could be further increased by elevating the operating temperature, as the peak position of the blackbody radiation peak blueshifts toward the visible range at higher operating temperatures (Wien's displacement law). The maximum luminous efficacy of the PRILD is projected as 236 lm/W at the operating temperature of 3782 K. This may be potentially realized by replacing the vacuum-filtered CNT film in the JTE with a highly graphitized, sonication-free CNT film (*24*).

We compare the luminous efficacy and lumen density of the PRILD with the state-of-the-art LED- and LD-based lighting devices (*25*, *26*) in Fig. 4D. The Auger recombination increases superlinearly with the increase of current density for LEDs, resulting in severe degradation of luminous efficacy at the current density higher than 10^2 A/cm^2. The Auger recombination also occurs near

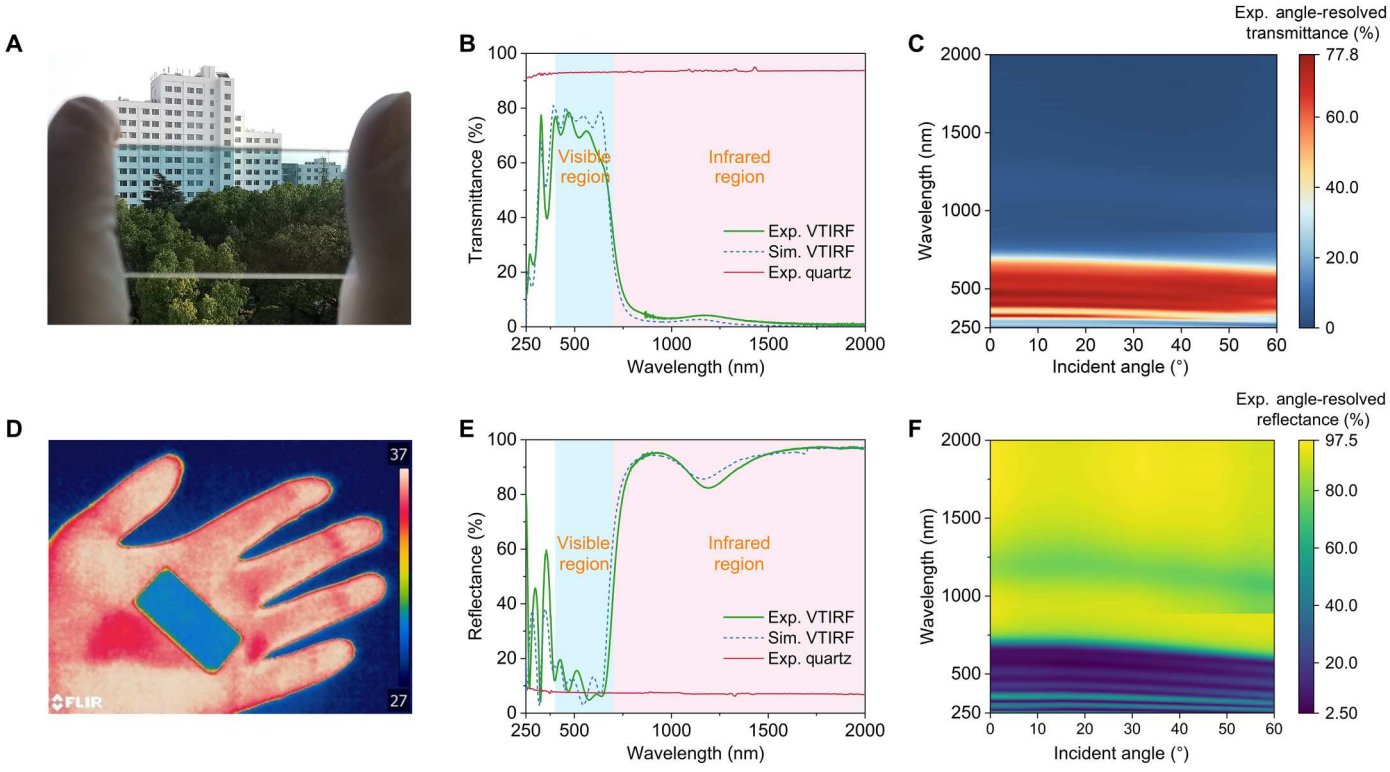

Fig. 3. Experimental characterization of the fabricated VTIRF window. (**A**) Photograph of the fabricated VTIRF window. (**B**) Experimental transmittance of the fabricated VTIRF window measured using the UV–visible (vis)–NIR spectroscopy with the integration sphere. The red solid line denotes the transmittance of the quartz substrate. The blue dashed line denotes the simulated transmittance of the designed VTIRF. (**C**) Experimental angle-resolved transmittance of the fabricated VTIRF window. (**D**) Infrared thermal imaging of the fabricated VTIRF window on the author's hand. The fabricated VTIRF window has the same temperature (37°C) with the hand yet shows similar emissivity with the cold background (27°C). (**E**) Experimental reflectance of the fabricated VTIRF window measured by the UV-vis-NIR spectroscopy with the integration sphere. The red solid line denotes the reflectance of the quartz substrate. The blue dashed line denotes the simulated reflectance of the designed VTIRF. (**F**) Experimental angle-resolved reflectance of the fabricated VTIRF window.

the lasing threshold of LD, causing a high threshold current density and high parasitic resistive losses, which, in turn, limits the luminous efficacy of the LD at the current density lower than 10^4 A/cm^2. Both LED- and LD-based lighting devices suffer from inherent Auger recombination and are inefficient at midrange current densities in between 10^2 and 10^4 A/cm^2, which is termed as "the valley of droop" (fig. S12). Our PRILD operates at the current density of 2.4 kA/cm^2 and lumen density of 48,087 lm/cm^2 at a luminous efficacy of 173.6 lm/W, while the lumen density of LEDs is ca. 2000 lm/cm^2 at the luminous efficacy of ca. 160 lm/W. The PRILD does not have the efficiency droop and the inherent Auger recombination in LEDs and LDs. Moreover, the operating current density of the PRILD could be tuned by varying the thickness and width of the JTE; thus, the PRILD has potential to operate at a wide range of the current densities.

We analyze the power flow distribution on the device level (fig. S13). The cavity loss includes thermal conduction loss from the JTE to the electrodes, thermal convection loss from the JTE to the cavity, and the thermal radiation absorbed by the cavity. The combination of the cavity loss and the Ohmic loss accounts for 25.4% of the total power input, resulting in an electrothermal conversion efficiency of 74.6%. The absorption-induced heat dissipation of the VTIRF window takes an additional 6.1% loss in power. Thus, the nonradiative dissipation loss in the PRILD accumulates to 31.5% of the total power input. For comparison, the nonradiative heat dissipation loss in the mainstream SSL takes 70 to 80% of the total power input (*4*) and thus requires active cooling. The major power loss of the PRILD is the radiative dissipation and comes from the mismatch between the peak of blackbody radiation curve at 2457 K and the peak of the photopic sensitivity curve, which accounts for 49.5% of the total power input. As the radiative dissipation is not accumulated in the device, the PRILD does not require active cooling even at power density of hundreds of watts per square centimeter. Moreover, the radiative power loss could be potentially harvested by the infrared photovoltaics as ubiquitous power supplies for internet of things.

We further carry out the durability tests on the fabricated PRILD. The CNTs and hBN in the JTE are inherently stable at high temperatures owing to the conjugated π-bond and the ceramic nature. In incandescent lamps, Edison and Coolidge changed from carbonized paper filaments to tungsten filaments to avoid evaporation of carbon back in the early 20th century. The CNTs used in this work have high graphitization (crystallinity) level, low defect level, and excellent thermal stability (figs. S14 and S15), which are fundamentally different from the carbonized paper used by Edison (note S1). We carry out CNT evaporation test at the operating temperature of the PRILD and detect no evaporation of carbon (fig. S16). The potential failure of the PRILD

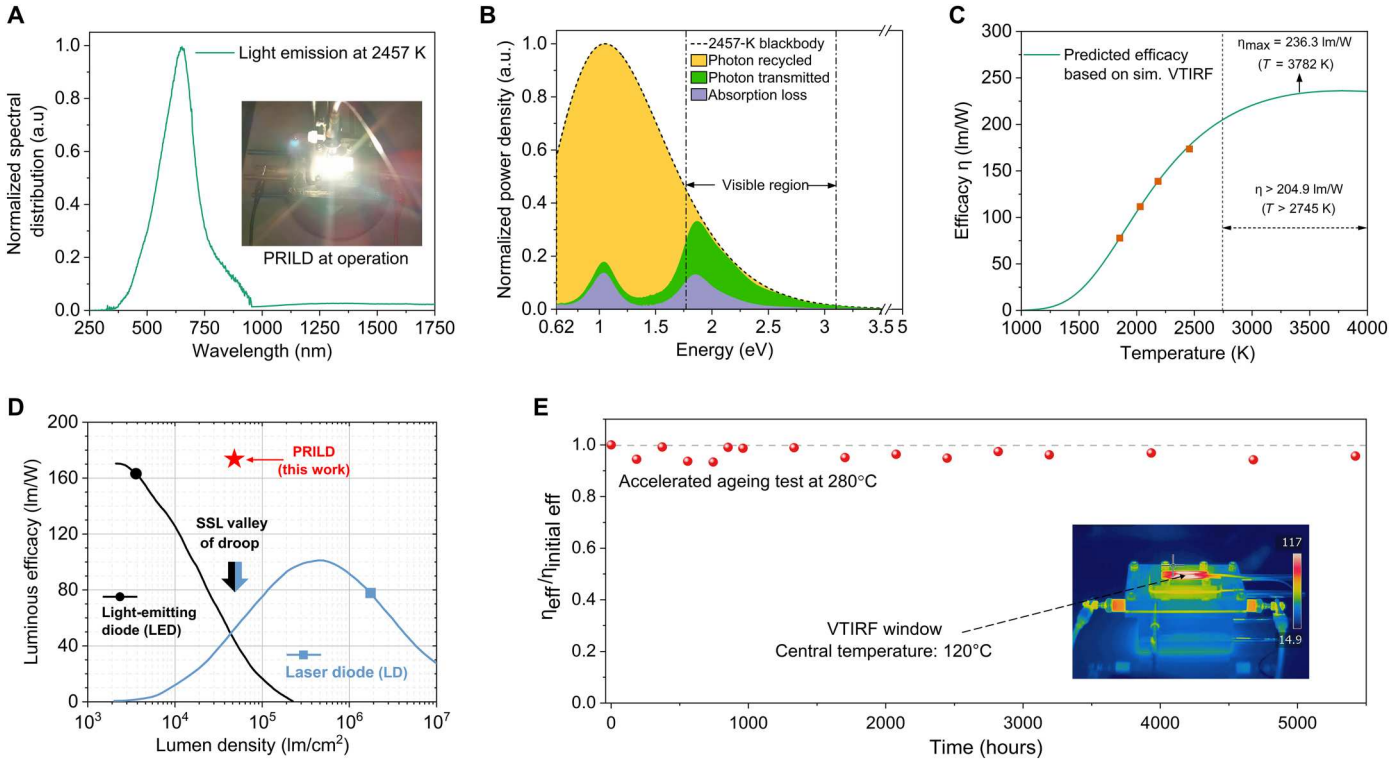

Fig. 4. Characterization of the PRLID. (**A**) Normalized light emission spectrum of the PRILD operating at 2457 K. The inset shows the photograph of the PRILD in operation. (**B**) Optical power distribution of the PRILD operating at 2457 K. The black dashed line shows the normalized power density of the blackbody at 2457 K. The fractions of the recycled photon energy, transmitted photon energy, and absorption loss are shaded in yellow, green, and violet, respectively. (**C**) Experimentally measured luminous efficacy (orange squares) and predicted luminous efficacy (green line) of the PRILD. (**D**) Luminous efficacy versus lumen density of the PRILD as well as LED- and LD-based lighting. The data of LED- and LD-based lighting are adopted from (*25*) and (*26*). (**E**) Accelerated aging tests of the VTIRF window at 280°C. The temperature at the center of the VTIRF window during operation is 120°C (without any cooling), as shown by the temperature distribution of the PRILD at operation in the inset.

mainly comes from the diffusion of the thin Ag-Ge alloy film in the VTIRF window at elevated temperatures. During operation (JTE at 2457 K), the highest temperature on the VTIRF window stabilizes at 120°C without using any cooling techniques, as measured by the infrared imaging and the thermocouple (the inset of Fig. 4E). We characterize the thermal stability of the fabricated VTIRF window under accelerated aging conditions at 280°C. According to the Arrhenius diffusion law (*27*), the surface diffusion rate of the thin Ag-Ge alloy film at 280°C is 15.49 times of that at 120°C. After 350 hours of accelerated aging test at 280°C (corresponding to 5422 hours at the operating temperature of the PRILD), the degradation in the luminous efficacy is negligible (Fig. 4E and fig. S17). Per the IES LT70 criteria, the lifetime of the PRILD is estimated as 66,896 hours.

DISCUSSION

On the basis of the experimentally obtained luminous efficacy and lifetime of the PRILD, we carry out life cycle assessment to evaluate the potential impact of the PRILD on the carbon emission (fig. S18). The raw materials used in one PRILD include Ge (0.001 mg/cm^2), Ag (0.023 mg/cm^2), SiO_2 (0.042 mg/cm^2), HfO_2 (0.171 mg/cm^2) (could be replaced with earth-abundant low-cost TiO_2), CNTs (4.42 mg/cm^2), hBN (16.98 mg/cm^2), and Al_2O_3 (ca. 83.33 mg/cm^2). The use of CNTs practices the concept of "use carbon to decarbonize" (*28*), which could solidify tons of CO_2 emissions per year by scalable deployment. To provide a light output of 20.3 Mlm·hour, the estimated life cycle carbon emission of the PRILD is 69.4 kgCO_2-eq, compared with 247.3 kgCO_2-eq for the mainstream LED-based lighting. The fabricated PRILD is a promising low–carbon emission, long-lifetime, high–luminous efficacy, and high–color rendition lighting technology operating at power density of hundreds of watts per square centimeter and thus fills the valley of droop in between LED- and LD-based lighting.

MATERIALS AND METHODS

Machine learning–enabled multiobjective design of the VTIRF

The optical properties of the VTIRF are calculated by the TMM. The machine learning algorithm for multiobjective optimization used in this work is the elitist NGSA-II (*21*). The ideal transmittance of the VTIRF $I(\lambda)$ and the three optimization objectives—obj_{eff},

obj_{CRI}, and obj_{loss}—are given as follows

$$I(\lambda) = \begin{cases} 1, 380\ \text{nm} \le \lambda \le 650\ \text{nm} \\ 0,\ \text{elsewhere} \end{cases} \quad (1)$$

$$obj_{eff} = \frac{\int_{380}^{2500} |I(\lambda) - t(\lambda)|\, d\lambda}{\int_{380}^{2500} d\lambda} \quad (2)$$

$$obj_{CRI} = \frac{\int_{380}^{650} |\bar{t} - t(\lambda)|\, d\lambda}{\int_{380}^{650} d\lambda} \quad (3)$$

$$obj_{loss} = \frac{\int_{380}^{2500} \alpha(\lambda) d\lambda}{\int_{380}^{2500} d\lambda} \quad (4)$$

where $I(\lambda)$ is the ideal transmittance curve, $t(\lambda)$ is the calculated transmittance of the designed VTIRF, $\bar{t}$ is the mean transmittance of the designed VTIRF in the visible range, and $\alpha(\lambda)$ is the calculated absorbance of the designed VTIRF.

The machine learning–enable multiobjective design process is as follows. First, the NGSA-II algorithm randomly generates the first generation of structures. Then, the TMM calculates the transmittance and absorption performance of the generated structures. The NGSA-II performs a nondominated sorting and identifies the Pareto optimal sets based on the three objectives. Then, the NGSA-II creates offspring generation structures from the Pareto optimal sets through evolution and sends these structures to TMM again. The framework iterates until the satisfactory Pareto optimal solution sets are obtained.

Field distribution calculation of the VTIRF

The distribution of the electric field, magnetic field, and Poynting vector on the designed VTIRF are calculated by finite difference time domain method using Lumerical FDTD Solutions. The wavelength range of the light source is from 250 to 2500 nm. The boundary condition on the *x* axis and the *y* axis is periodic boundary condition. The boundary condition on the *z* axis is perfectly matched layer. The mesh size in the three dimensions is 1 nm.

Sample fabrication

Fabrication of the VTIRF window

The quartz substrate with a size of 25 mm by 50 mm is cleaned by bath ultrasonication using acetone, ethanol, and deionizing water for 10 min. The Al_2O_3 and HfO_2 layers are deposited by atomic layer deposition (R200, PICOSUN) at 255°C using trimethylaluminum (Strem Chemicals) and tetrakis(dimethylamido)hafnium(IV) (Strem Chemicals) as precursors, respectively. The oxidizing agent is H_2O. The precursor carrier gas is N_2 (99.999% purity, Shanghai Weichuang Gas). The Ag-Ge alloy and SiO_2 layers are deposited by electron beam evaporation (PVD 75, Kurt J. Lesker) in vacuum.

Fabrication of the JTE

The CNT powders (Ordos Xin-Ao Nanocarbon Materials) are dispersed in aqueous solution using SDS (Aladdin) as the dispersant by probe sonication (KS-150 N, Shanghai KeQi Instrument). The CNT film (black emitter) is prepared by vacuum filtration of the dispersed CNT aqueous solution. The hBN coating (white emitter) is sprayed on the top of the CNT film to form the JTE. Then, the JTE is dried in oven for 12 hours and cut into the size of 27 mm by 3 mm.

Assembly of the PRILD

The two ends of the JTE are clamped with copper rod electrodes that are connected to a power supply. The dispersant in the JTE is removed by Joule heating at 800°C in argon environment. Then, JTE is annealed at about 2500 K to remove defects of CNT to improve the high-temperature stability of JTE. The JTE is suspended in the center of the CCC (custom-made from DiamondTec). The VTIRF window covers on top of the CCC. The PRILD cavity is sealed by rubber o-rings and filled with argon to protect the oxidation of the JTE and the VTIRF.

Characterizations

Experimental measurement of the optical constants

The refractive index (n) and extinction coefficient (k) of the materials used in the VTIRF are characterized by the variable-angle spectroscopic ellipsometer (RC2-II, J. A. Woollam) from 190 to 1700 nm at the incident angles of 55°, 65°, and 75°. The optical constants in the range from 1700 to 2500 nm are obtained by linear fitting and extrapolation and are eventually verified by the experimental measurement of the transmittance and reflectance of the fabricated samples.

Experimental measurement of transmittance and reflectance

The transmittance and reflectance spectra at the normal incident angle are measured by UV-visible-NIR spectrophotometer (Lambda 950, PerkinElmer) with the integrating sphere accessory. Angle-resolved transmission and reflection spectra are measured by the same spectrophotometer using an angular optical bench and a universal reflectance accessory, respectively.

Temperature measurement of the JTE

The temperature of the JTE during operation is measured using the infrared high-speed noncontact pyrometer probe (IGA 740, IMPAC). The electrical resistances of the JTE at different operating temperatures are recorded by a power meter (Agilent). The relationship between the temperature and the resistance of the JTE during operation is given in fig. S9.

Surface morphology measurement of the VTIRF window

The surface morphology of the VTIRF window is characterized by atomic force microscopy (MultiMode8, Bruker).

Thermal stability measurement of the VTIRF window

The potential failure of the VTIRF window comes from the diffusion and grain growth of the Ag-Ge alloy thin film in the fabricated VTIRF window. The diffusion of Ag-Ge alloy is expressed as

$$D = D_0 e^{-\frac{E_{AgGe}}{KT}} \quad (5)$$

where D_0 is diffusion constant and E_{AgGe} is the activation energy for the Ag-Ge diffusion. We carry out the accelerated aging tests by annealing at 280°C under atmospheric pressure in argon environment (MTI Kejing). The central temperature of the VTIRF window during the PRILD operation is 120°C, which is the average value of the infrared thermal camera and thermocouple. The surface

diffusion rate of the Ag-Ge alloy thin film at 280°C is 15.49 times of that at 120°C. The transmittance of the VTIRF window after 280°C accelerated aging is measured to evaluate the performance degradation.

Experimental characterization of the PRILD

The measurement is carried out in argon environment to avoid the absorption from the air. The optical fiber probe with a collimation mirror is fixed vertically above the PRILD. The emission spectra in the wavelength ranges of 200 to 1000 nm and 900 to 1750 nm are measured by IdeaOptics PG2000-Pro and NIR-17S, respectively. The CRI, CCT, and color coordinates are calculated from the measured emission spectrum. The luminous efficacy of a lighting source is related to the sensitivity of the human eye, which is the ratio of the visible light energy to the total radiant energy, as follows

$$\eta = \frac{V_{\max}(\lambda)\int_0^{\infty} I(\lambda,T)V_n(\lambda)d\lambda}{\int_0^{\infty} I(\lambda,T)d\lambda} \quad (6)$$

where η is the luminous efficacy of a lighting source, λ is the wavelength, T is the temperature, $I(\lambda, T)$ is the spectral radiative power of a lighting source, $V_n(\lambda)$ is the normalized photopic luminosity function, and $V_{\max}(\lambda)$ is the maximum value of the photopic luminosity function (683 lm/W).

Lifetime evaluation of the PRILD

The lifetime of PRILD is evaluated by the following logarithmic function

$$\frac{\eta_{\text{eff}}}{\eta_{\text{initial eff}}} = \ln(a + bt) \quad (7)$$

where η_{eff} is the luminous efficacy after accelerated aging, $\eta_{\text{initial eff}}$ is the original luminous efficacy, a and b are fitting parameters, and t is estimated lifetime of the PRILD. L70 lifetime is the estimated lifetime of the lighting device when $\eta_{\text{eff}}/\eta_{\text{initial eff}}$ is 0.7.

Supplementary Materials

This PDF file includes:

Note S1
Figs. S1 to S18
Table S1
References

REFERENCES AND NOTES

1. IEA, World Energy Outlook 2021, (IEA, Paris 2021); www.iea.org/reports/world-energy-outlook-2021.
2. J. Chen, S. Mukherjee, W. Li, H. Zeng, R. A. Fischer, Bespoke crystalline hybrids towards the next generation of white LEDs. *Nat. Rev. Mater.* **7**, 677–678 (2022).
3. J. J. Wierer Jr., J. Y. Tsao, D. S. Sizov, Comparison between blue lasers and light-emitting diodes for future solid-state lighting. *Laser Photonics Rev.* **7**, 963–993 (2013).
4. X. Luo, R. Hu, S. Liu, K. Wang, Heat and fluid flow in high-power LED packaging and applications. *Prog. Energy Combust. Sci.* **56**, 1–32 (2016).
5. Y. H. Kim, P. Arunkumar, B. Y. Kim, S. Unithrattil, E. Kim, S. H. Moon, J. Y. Hyun, K. H. Kim, D. Lee, J. S. Lee, W. B. Im, A zero-thermal-quenching phosphor. *Nat. Mater.* **16**, 543–550 (2017).
6. T. W. Davies, T. Smyth, Why artificial light at night should be a focus for global change research in the 21st century. *Glob. Chang. Biol.* **24**, 872–882 (2018).
7. M. A. Contin, M. M. Benedetto, M. L. Quinteros-Quintana, M. E. Guido, Light pollution: The possible consequences of excessive illumination on retina. *Eye* **30**, 255–263 (2016).
8. P. Geiger, M. Barben, C. Grimm, M. Samardzija, Blue light-induced retinal lesions, intraretinal vascular leakage and edema formation in the all-cone mouse retina. *Cell Death Dis.* **6**, e1985 (2015).
9. E. Knop, L. Zoller, R. Ryser, C. Gerpe, M. Horler, C. Fontaine, Artificial light at night as a new threat to pollination. *Nature* **548**, 206–209 (2017).
10. C. C. M. Kyba, Is light pollution getting better or worse? *Nat. Astron.* **2**, 267–269 (2018).
11. D. H. Boyes, D. M. Evans, R. Fox, M. S. Parsons, M. J. O. Pocock, Street lighting has detrimental impacts on local insect populations. *Sci. Adv.* **7**, eabi8322 (2021).
12. S. Kubba, *Handbook of Green Building Design and Construction* (Butterworth-Heinemann, 2012).
13. P. M. Pattison, J. Y. Tsao, G. C. Brainard, B. Bugbee, LEDs for photons, physiology and food. *Nature* **563**, 493–500 (2018).
14. O. Ilic, P. Bermel, G. Chen, J. D. Joannopoulos, I. Celanovic, M. Soljacic, Tailoring high-temperature radiation and the resurrection of the incandescent source. *Nat. Nanotechnol.* **11**, 320–324 (2016).
15. A. Leroy, B. Bhatia, K. Wilke, O. Ilic, M. Soljačić, E. N. Wang, Combined selective emitter and filter for high performance incandescent lighting. *Appl. Phys. Lett.* **111**, 094103 (2017).
16. H. Wang, Z. Zheng, C. Ji, L. J. Guo, Automated multi-layer optical design via deep reinforcement learning. *Mach. Learn. Sci. Technol.* **2**, 025013 (2021).
17. J. F. Varner, D. Wert, A. Matari, R. Nofal, J. J. Foley IV, Accelerating the discovery of multilayer nanostructures with analytic differentiation of the transfer matrix equations. *Phys. Rev. Res.* **2**, 013018 (2020).
18. K. Cui, B. L. Wardle, Breakdown of native oxide enables multifunctional, free-form carbon nanotube-metal hierarchical architectures. *ACS Appl. Mater. Inter.* **11**, 35212–35220 (2019).
19. J. H. Los, K. V. Zakharchenko, M. I. Katsnelson, A. Fasolino, Melting temperature of graphene. *Phys. Rev. B.* **91**, 045415 (2015).
20. J. D. Caldwell, I. Aharonovich, G. Cassabois, J. H. Edgar, B. Gil, D. N. Basov, Photonics with hexagonal boron nitride. *Nat. Rev. Mater.* **4**, 552–567 (2019).
21. K. Deb, A. Pratap, S. Agarwal, T. Meyarivan, A fast and elitist multiobjective genetic algorithm NSGA-II. *IEEE Trans. Evol. Comput.* **6**, 182–197 (2002).
22. S. K. Shevell, *The Science of Color* (Elsevier Science, 2nd ed., 2003).
23. W. E. Forsythe, M. A. Easley, D. D. Hinman, Time constants of incandescent lamps. *J. Appl. Phys.* **9**, 209–214 (1938).
24. X. Wei, M. S. Wang, Y. Bando, D. Golberg, Thermal stability of carbon nanotubes probed by anchored tungsten nanoparticles. *Sci. Technol. Adv. Mater.* **12**, 044605 (2011).
25. J. J. Wierer Jr., N. Tansu, A. J. Fischer, J. Y. Tsao, III-nitride quantum dots for ultra-efficient solid-state lighting. *Laser Photonics Rev.* **10**, 612–622 (2016).
26. U.S. Department of Energy, *2022 Solid State Lighting R&D Opportunities* (Energy Efficiency & Renewable Energy, 2022).
27. H. C. Kim, T. L. Alford, D. R. Allee, Thickness dependence on the thermal stability of silver thin films. *Appl. Phys. Lett.* **81**, 4287–4289 (2002).
28. M. Pasquali, C. Mesters, Opinion: We can use carbon to decarbonize-and get hydrogen for free. *Proc. Natl. Acad. Sci. U.S.A.* **118**, e2112089118 (2021).
29. U.S. Department of Energy, *Life-Cycle Assessment of Energy and Environmental Impacts of LED Lighting Products Part 2: LED Manufacturing and Performance* (Pacific Northwest National Laboratory, 2012).
30. U.S. Department of Energy, *Solid-State Lighting 2017 Suggested Research Topics Supplement: Technology and Market Context* (Energy Efficiency & Renewable Energy, 2017).

Acknowledgments

Funding: This work is sponsored by the Shanghai Pujiang Program (19PJ1404600 to K.C.) and Shanghai Sailing Program (21YF1419700 to Z.H.) from the Science and Technology Commission of Shanghai Municipality, and the startup funding (WF220405012 to K.C.) from SJTU. This research made use of the shared facilities of Zhiyuan Innovative Research Center (ZIRC) at SJTU, Center for Advanced Electronic Materials and Devices (AEMD) and Instrumental Analysis Center (IAC) at SJTU. **Author contributions:** Conceptualization: K.C. Methodology: H.Z., Z.H., M.D., and K.C. Investigation: H.Z., Z.H., M.D., Q.W., Y.F., Z.L., S.W., L.Y., S.C., W.S., J.Z., T.D., H.X., and K.C. Visualization: H.Z., Z.H., and K.C. Funding acquisition: K.C. and Z.H. Project administration: K.C. Supervision: K.C. Writing—original draft: H.Z. and K.C. Writing—review and editing: H.Z., Z.H., H.X., and K.C. **Competing interests:** K.C., H.Z., and Z.H. are inventors on two pending patents related to this work filed by Shanghai Jiao Tong University (nos. 202310122486.5 and 202310122478.0, filed 16 February 2023). The authors declare that they have no other competing interests. **Data and materials availability:** All data needed to evaluate the conclusions in the paper are present in the paper and/or the Supplementary Materials.

Submitted 17 October 2022
Accepted 10 March 2023
Published 12 April 2023
10.1126/sciadv.adf3737